AGU PUBLICATIONS

JGR

Journal of Geophysical Research: Space Physics

RESEARCH ARTICLE
10.1002/2015JA022134

Key Points:
- Alfven-cyclotron and ion Bernstein instabilities driven by a proton shell velocity distribution
- The maximum linear growth of Alfven-cyclotron waves is smaller than that of Bernstein modes
- Yet the Alfven-cyclotron waves can saturate at a larger level even with a moderate anisotropy

Supporting Information:
- Supporting Information S1

Correspondence to:
K. Min,
kmin@auburn.edu

Citation:
Min, K., K. Liu, and S. Peter Gary (2016), Scalings of Alfvén-cyclotron and ion Bernstein instabilities on temperature anisotropy of a ring-like velocity distribution in the inner magnetosphere, *J. Geophys. Res. Space Physics*, *121*, 2185–2193, doi:10.1002/2015JA022134.

Received 9 NOV 2015
Accepted 18 FEB 2016
Accepted article online 20 FEB 2016
Published online 18 MAR 2016

Scalings of Alfvén-cyclotron and ion Bernstein instabilities on temperature anisotropy of a ring-like velocity distribution in the inner magnetosphere

Kyungguk Min[1], Kaijun Liu[1], and S. Peter Gary[2]

[1]Department of Physics, Auburn University, Auburn, Alabama, USA, [2]Space Science Institute, Boulder, Colorado, USA

Abstract A ring-like proton velocity distribution with $\partial f_p(v_\perp)/\partial v_\perp > 0$ and which is sufficiently anisotropic can excite two distinct types of growing modes in the inner magnetosphere: ion Bernstein instabilities with multiple ion cyclotron harmonics and quasi-perpendicular propagation and an Alfvén-cyclotron instability at frequencies below the proton cyclotron frequency and quasi-parallel propagation. Recent particle-in-cell simulations have demonstrated that even if the maximum linear growth rate of the latter instability is smaller than the corresponding growth of the former instability, the saturation levels of the fluctuating magnetic fields can be greater for the Alfvén-cyclotron instability than for the ion Bernstein instabilities. In this study, linear dispersion theory and two-dimensional particle-in-cell simulations are used to examine scalings of the linear growth rate and saturation level of the two types of growing modes as functions of the temperature anisotropy $T_\perp/T_{||}$ for a general ring-like proton distribution with a fixed ring speed of $2v_A$, where v_A is the Alfvén speed. For the proton distribution parameters chosen, the maximum linear theory growth rate of the Alfvén-cyclotron waves is smaller than that of the fastest-growing Bernstein mode for the wide range of anisotropies ($1 \le T_\perp/T_{||} \le 7$) considered here. Yet the corresponding particle-in-cell simulations yield a higher saturation level of the fluctuating magnetic fields for the Alfvén-cyclotron instability than for the Bernstein modes as long as $T_\perp/T_{||} \gtrsim 3$. Since fast magnetosonic waves with ion Bernstein instability properties observed in the magnetosphere are often not accompanied by electromagnetic ion cyclotron waves, the results of the present study indicate that the ring-like proton distributions responsible for the excitation of these fast magnetosonic waves should not be very anisotropic.

1. Introduction

Two classes of enhanced fluctuations frequently observed in the inner magnetosphere with frequency on the order of Ω_p, the proton cyclotron frequency, are electromagnetic ion cyclotron (EMIC) waves and fast magnetosonic waves [e.g., *Anderson et al.*, 1992; *Meredith et al.*, 2008], which have as their source Alfvén-cyclotron and ion Bernstein instabilities, respectively [e.g., *Gary et al.*, 2010, 2012]. Both types of waves are driven by interactions with ring current ions, but their sources of free energy, properties, and effects on the plasma medium are substantially different.

Alfvén-cyclotron instabilities are excited by anisotropic distributions ($T_\perp/T_{||} > 1$) of injected energetic ring current ions and have maximum instability growth rate at $\mathbf{k} \times \mathbf{B}_0 = 0$ [e.g., *Cornwall*, 1965; *Chen et al.*, 2010a], where $\mathbf{k}$ is the wave number and $\mathbf{B}_0$ is the background magnetic field and $T_\perp$ and $T_{||}$ are temperatures, respectively, perpendicular and parallel to $\mathbf{B}_0$. The enhanced magnetic fluctuations from these growing modes are predominantly left-hand polarized and can lead to precipitation of energetic ring current ions and relativistic radiation belt electrons through pitch angle scattering [e.g., *Thorne*, 2010].

Ion Bernstein instabilities, on the other hand, are excited by proton velocity distributions with $\partial f_p(v_\perp)/\partial v_\perp > 0$ [e.g., *Perraut et al.*, 1982; *McClements et al.*, 1994; *Horne et al.*, 2000; *Gary et al.*, 2011; *Balikhin et al.*, 2015] formed by energy-dependent drift of the injected ring current ions [*Chen et al.*, 2010a, 2010b]. These instabilities can be driven both by isotropic velocity shell distributions [e.g., *Gary et al.*, 2010] and by anisotropic ring-like velocity distributions [e.g., *McClements et al.*, 1994]. The resulting enhanced fluctuations often exhibit distinct proton cyclotron harmonic dispersion [e.g., *Balikhin et al.*, 2015], have their maximum growth rates at

propagation quasi-perpendicular to $\mathbf{B}_0$, and are characterized with $|\delta B_{||}/\delta \mathbf{B}| \sim 1$ and $|\delta E_{\mathbf{k}}/\delta \mathbf{E}| \sim 1$ [*Denton et al.*, 2010; *Gary et al.*, 2010, 2011; *Min and Liu*, 2015a], where $\delta\mathbf{E}$ and $\delta\mathbf{B}$ are electric and magnetic field fluctuations, respectively, and $\delta E_{\mathbf{k}} \equiv \delta\mathbf{E}\cdot\mathbf{k}/|\mathbf{k}|$. Fast magnetosonic waves not only lead to scattering of background and ring current ions in the perpendicular velocity component but also play a role in the acceleration to relativistic energies of radiation belt electrons and in the detrapping of such electrons [*Horne et al.*, 2007; *Bortnik and Thorne*, 2010; *Chen et al.*, 2015].

A sufficiently anisotropic ring-like proton velocity distribution can be unstable to both the ion Bernstein and Alfvén-cyclotron instabilities. *Min and Liu* [2016] (referred to as paper 1 hereinafter) performed comprehensive analyses of both instabilities simultaneously driven by ring velocity distributions using linear dispersion theory and two-dimensional electromagnetic particle-in-cell (PIC) simulations. For the proton ring velocity distributions considered in paper 1, although the maximum linear theory growth rate of the Alfvén-cyclotron instability was consistently smaller than the theoretical growth rate of the fastest-growing Bernstein mode, the PIC simulations consistently yielded larger saturation amplitudes for the Alfvén-cyclotron instability. In one case examined therein, the maximum growth rate of the Alfvén-cyclotron instability is smaller by a factor of 3 than that of the ion Bernstein instability, and yet the saturation level of the former waves is larger at least by an order of magnitude.

There is an abundant literature on the frequent magnetospheric observations of fast magnetosonic waves [*Santolík et al.*, 2004; *Němec et al.*, 2005, 2006, 2013; *Meredith et al.*, 2008; *Ma et al.*, 2013; *Boardsen et al.*, 2014; *Zhou et al.*, 2014; *Hrbáčková et al.*, 2015; *Xiao et al.*, 2015] and EMIC waves [*Anderson et al.*, 1992; *Fraser and Nguyen*, 2001; *Fraser et al.*, 2010; *Halford et al.*, 2010; *Clausen et al.*, 2011; *Usanova et al.*, 2012; *Min et al.*, 2012; *Allen et al.*, 2015; *Saikin et al.*, 2015]. However, to our knowledge, there have been few reports on the simultaneous observation of EMIC and fast magnetosonic waves [cf. *Rodger et al.*, 2015, Figures 1 and 2]. *Posch et al.* [2015] recently presented a survey of the low-frequency ($\sim \Omega_p$) fast magnetosonic waves. Although they did not explicitly examine the EMIC waves in association with the fast magnetosonic waves, their figures of electric and magnetic field wave spectra of the selected events do not suggest substantial EMIC wave power comparable to fast magnetosonic wave power. In fact, of the entire events of the fast magnetosonic waves identified from electric and magnetic field data over the first full local time precession of both Van Allen Probes [*Mauk et al.*, 2013], only one event was approximately accompanied by weak EMIC waves (M. J. Engebretson, E-mail discussions about the statistical probability of the simultaneous occurrences of EMIC and fast magnetosonic waves, private communication, 2015). Thus, the ring-like velocity distributions associated with fast magnetosonic waves in the inner magnetosphere [*Meredith et al.*, 2008; *Ma et al.*, 2013] should be more isotropic than the ring distributions analyzed in paper 1.

The goal of the present study is to investigate how the linear growth and nonlinear saturation of Alfvén-cyclotron and ion Bernstein instabilities driven by a proton ring-like velocity distribution vary with the temperature anisotropy of that distribution. In particular, this study aims to determine the critical anisotropy for the two instabilities to saturate at the same level. This critical anisotropy should represent an upper anisotropy limit of the proton ring-like distributions responsible for the observed fast magnetosonic waves in the magnetosphere which are often not accompanied by EMIC waves. The paper is organized as follows. Section 2 describes the two-component proton velocity distribution, some basic information of the linear analyses, and the setup of the PIC simulations. Section 3 presents the results, and section 4 concludes the paper.

Following paper 1, we denote the jth species plasma frequency as $\omega_j \equiv \sqrt{4\pi n_j e^2/m_j}$, the jth species cyclotron frequency as $\Omega_j \equiv e_j B_0/m_j c$, and the jth component beta as $\beta_j \equiv 8\pi n_j T_j/B_0^2$ and $\tilde{\beta}_j \equiv 8\pi n_0 T_j/B_0^2$. The Alfvén speed is $v_A \equiv B_0/\sqrt{4\pi n_0 m_p}$, the proton inertial length is $\lambda_p \equiv \sqrt{m_p c^2/4\pi n_0 e^2}$, and the lower hybrid frequency is $\omega_{\mathrm{lh}} = \omega_p/\sqrt{1+\omega_e^2/\Omega_e^2}$. Here n_0 is equal to the unperturbed electron density n_e. Also, we adopt the reduced proton-to-electron mass ratio of $m_p/m_e = 100$ and the relatively small light-to-Alfvén speed ratio of $c/v_A = 15$ to make the computational cost of the PIC simulations affordable. These reduced parameters reduce the lower hybrid frequency $\omega_{\mathrm{lh}} \approx 8.3\Omega_p$ and thereby the number of harmonics of fast magnetosonic waves.

2. Methodology

In order to effectively examine the instability scaling on the temperature anisotropy of the ring-like proton velocity distribution, a base distribution function has been constructed so that its anisotropy can be freely adjusted while other parameters are held constant. The base distribution function used is

$$f_j(v,\alpha) \equiv \frac{n_j}{\pi^{3/2}\theta_j^3 C_j} e^{-(v-v_j)^2/\theta_j^2} \sin^{\sigma_j}\alpha, \tag{1}$$

which we label "partial shell" distribution. Here α is the pitch angle, $v \equiv \sqrt{v_\perp^2 + v_{||}^2}$, v_j and θ_j are jth component's shell speed and thermal spread of the shell, respectively, $\sigma_j \geq 0$ is jth component's degree of anisotropy, and jth component's normalization constant is

$$C_j = \left[\frac{v_j}{\theta_j}\exp\left(-\frac{v_j^2}{\theta_j^2}\right) + \sqrt{\pi}\left(\frac{1}{2}+\frac{v_j^2}{\theta_j^2}\right)\left(1+\mathrm{erf}(v_j/\theta_j)\right)\right]\frac{\Gamma(1+\sigma_j/2)}{\Gamma(1.5+\sigma_j/2)},$$

where $\Gamma(x) \equiv \int_0^\infty t^{x-1}e^{-t}\mathrm{d}t$ is the Euler gamma function [*Arfken*, 1985, chap. 10] and $\mathrm{erf}(x) \equiv 2/\sqrt{\pi}\int_0^x e^{-t^2}\mathrm{d}t$ is the error function [*Arfken*, 1985, pp. 568–569]. We define the effective parallel and perpendicular temperatures [*Gary*, 1993, pp. 3–4] of the jth component as

$$T_{||j} \equiv \frac{m_j}{n_j}\int v_{||}^2 f_j \mathrm{d}^3\mathbf{v} \text{ and } T_{\perp j} \equiv \frac{m_j}{2n_j}\int v_\perp^2 f_j \mathrm{d}^3\mathbf{v}. \tag{2}$$

Then jth component's temperature anisotropy is simply

$$\frac{T_{\perp j}}{T_{||j}} = \frac{\sigma_j + 2}{2}. \tag{3}$$

Note for $v_j > 0$ and $\sigma_j = 0$ that equation (1) represents the isotropic shell velocity distribution used in *Liu et al.* [2011] and *Min and Liu* [2015a, 2015b]. For sufficiently large σ_j the distribution peaks at $v_{||} = 0$ and becomes close to the ring distribution used in paper 1.

As in paper 1, we consider a two-component proton velocity distribution of the form $f_p(\mathbf{v}) = f_M(v,\alpha) + f_r(v,\alpha)$, where each component is represented by equation (1). The first component f_M represents a thermal Maxwellian proton background with $v_M = \sigma_M = 0$ and $\tilde{\beta}_M = \theta_M^2/v_A^2 = 0.002$ in equation (1). The second component f_r represents the partial shell proton velocity distribution (i.e., $v_r > 0$) with $\theta_r^2/v_A^2 = 0.2$. We choose $v_r/v_A = 2$ and $n_r/n_e = 0.1$ because, as suggested by paper 1, these parameters should result in unstable Bernstein modes across all harmonics and sufficiently large instability growth rates to simulate the two types of waves within reasonable computational times. Additionally, electrons are represented by a Maxwellian with $\beta_e = \tilde{\beta}_M$. In the present study, the only parameter allowed to vary is σ_r, which effectively controls the temperature anisotropy of the partial shell protons, $T_{\perp r}/T_{||r}$, through equation (3). As listed in Table 1, a wide range of σ_r values between 0 and 12 (correspondingly $1 \leq T_{\perp r}/T_{||r} \leq 7$) are considered for our linear analyses and PIC simulations discussed in the next section.

Since the dispersion solver [*Min and Liu*, 2015b] to be used is based on ring beam velocity distributions and does not directly accept the partial shell distribution, f_r, of equation (1), we approximate f_r with multiple ring beam distributions as follows [*Min and Liu*, 2015b]:

$$f_r(v,\alpha) \approx n_r \sum_{l=-1}^{N+1} \frac{\eta_l}{\pi^{3/2}\theta_r^3 A_l} e^{-\left(v_{||}-v'_{d,l}\right)^2/\theta_r^2} e^{-\left(v_\perp - v'_{r,l}\right)^2/\theta_r^2}, \tag{4}$$

where $v_{||} = v\cos\alpha$, $v_\perp = v\sin\alpha$, $v'_{d,l} = v'_r\cos(l\Delta\phi)$, $v'_{r,l} = v'_r\sin(l\Delta\phi)$, and

$$A_l = \exp\left(-v'^2_{r,l}/\theta_r^2\right) + \sqrt{\pi}\left(v'_{r,l}/\theta_r\right)\left(1+\mathrm{erf}\left(v'_{r,l}/\theta_r\right)\right) \text{ and}$$
$$\eta_l = A_l \sin^{\sigma'_r}(l\Delta\phi)/\sum_{k=-1}^{N+1} A_k \sin^{\sigma'_r}(k\Delta\phi).$$

Table 1. Parameters of Two-Component Proton Distribution[a] and Summary of Linear Analyses Results

σ_r	$T_{\perp r}/T_{\|\|r}$	v_r'	σ_r'	ω_m^{AC}/Ω_p	$k_m^{AC}\lambda_p$	ψ_m^{AC}	ω_m^{IB}/Ω_p	$k_{\perp m}^{IB}\lambda_p$	$k_{\|\|m}^{IB}\lambda_p$	PIC
0	1	2.024	0	$0.464 + 4.85 \cdot 10^{-4}i$	1.47	70°	$2.94 + 0.0788i$	3.3	0.1	○
0.5	1.25	2.024	0.451	$0.445 + 2.52 \cdot 10^{-3}i$	1.39	70°	$2.96 + 0.0910i$	3.35	0.07	×
1	1.5	2.024	1.004	$0.416 + 5.82 \cdot 10^{-3}i$	1.28	70°	$2.97 + 0.104i$	3.37	0.04	○
1.5	1.75	2.024	1.560	$0.341 + 0.0122i$	0.41	0°	$2.97 + 0.115i$	3.37	≤ 0.01	×
2	2	2.024	2.12	$0.363 + 0.0216i$	0.443	0°	$2.96 + 0.123i$	3.36	≤ 0.01	○
3	2.5	2.023	3.313	$0.385 + 0.0352i$	0.47	0°	$2.96 + 0.134i$	3.34	≤ 0.01	○
4	3	2.022	4.56	$0.410 + 0.0452i$	0.51	0°	$2.95 + 0.139i$	3.32	≤ 0.01	○
5	3.5	2.021	5.88	$0.438 + 0.0545i$	0.565	0°	$2.94 + 0.142i$	3.3	≤ 0.01	○
6	4	2.021	7.275	$0.453 + 0.0629i$	0.59	0°	$2.94 + 0.143i$	3.29	≤ 0.01	○
7	4.5	2.020	8.75	$0.462 + 0.0700i$	0.605	0°	$2.94 + 0.144i$	3.28	≤ 0.01	×
8	5	2.019	10.315	$0.472 + 0.0759i$	0.62	0°	$2.94 + 0.144i$	3.27	≤ 0.01	×
9	5.5	2.018	11.981	$0.479 + 0.0809i$	0.63	0°	$2.93 + 0.144i$	3.26	≤ 0.01	○
10	6	2.017	13.752	$0.486 + 0.0851i$	0.64	0°	$2.93 + 0.144i$	3.26	≤ 0.01	×
11	6.5	2.016	15.644	$0.493 + 0.0887i$	0.65	0°	$8.78 + 0.145i$	6.58	1.7	×
12	7	2.015	17.668	$0.500 + 0.0917i$	0.665	0°	$8.76 + 0.149i$	6.54	1.7	○

[a] All other parameters fixed are $\theta_r^2/v_A^2 = 0.2$, $\beta_e = \tilde{\beta}_M = 0.002$, $n_r/n_e = 0.1$, and $n_M/n_e = 0.9$.

Here A_l is the normalization constant for lth component's ring beam distribution function (the term inside the summation in equation (4)) and η_l represents contribution of the lth ring beam component such that $\sum_l \eta_l = 1$. For fixed $N = 12$, we get $\Delta\phi = 180°/N = 15°$; the choice of N is empirical to make a smooth pitch angle profile of the approximate f_r [e.g., *Min and Liu*, 2015b, Figure 1]. The values v_r' and σ_r' are chosen to minimize the visual difference between exact and approximate f_r contour plots and the difference between exact and approximate $T_{\perp r}/T_{\|\|r}$; minimizing the latter difference is particularly important because the Alfvén-cyclotron instability is directly related to the temperature anisotropy [e.g., *Kennel and Petschek*, 1966]. The approximate $T_{\perp r}/T_{\|\|r}$ is obtained from the ratio of the perpendicular-to-parallel second velocity moments $\langle v_\perp^2\rangle/\langle 2v_\|^2\rangle$ (using equation (2)) of the approximate f_r of equation (4). Table 1 lists the v_r' and σ_r' values determined manually; in all cases the relative differences of the exact and approximate $T_{\perp r}/T_{\|\|r}$ are less than 10^{-3}. Figure 1 displays comparison of contours of the exact (solid gray) and approximate (dashed red) f_r for $\sigma_r = 1, 6$, and 12, showing the two to be nearly identical.

For the selected cases as marked in Table 1 by circle in the last column, we carry out two-dimensional electromagnetic PIC simulations using the same code and the same setup as in paper 1, except that now energetic protons are initialized to have the partial shell distribution of equation (1) and that 10 times fewer simulation particles per species/component are used to decrease computational times. Compared with the simulations in paper 1, the fewer number of simulation particles leads to slightly higher thermal noise but does not obscure the main physics phenomena presented here. The simulation domain is contained in the x-y plane with the uniform background magnetic field $\mathbf{B}_0$ along the x direction, and periodic boundary conditions are used in both dimensions. We choose the simulation sizes $L_x = 120\lambda_p$ and $L_y = 48\lambda_p$, the number of cells $N_x = N_y = 960$, and the number of simulation particles per cell and component/species $N_c = 250$. The reduced

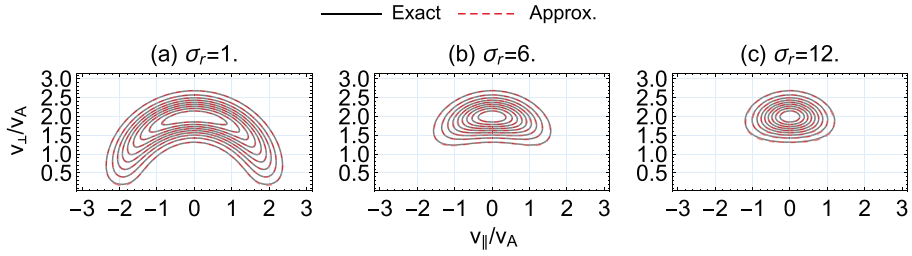

Figure 1. Comparison of the exact (equation (1)) and approximate (equation (4)) partial shell velocity distributions for $\sigma_r = 1$, 6 and 12.

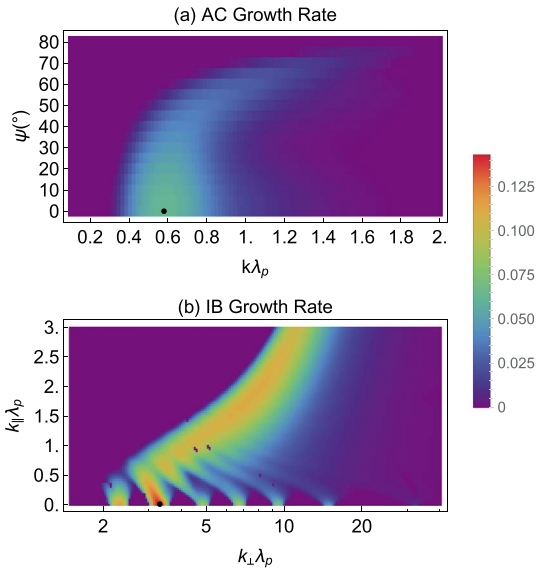

Figure 2. Linear theory growth rate corresponding to the (top) Alfvén-cyclotron and (bottom) ion Bernstein instabilities for $\sigma_r = 6$ (equivalently $T_{\perp r}/T_{||r} = 4$). The solid dots are located at the maximum growth rates for the respective instabilities (see Table 1).

$m_p/m_e = 100$ and rather small $c/v_A = 15$ enable a reasonably large simulation time step of $\Delta t = 0.001\Omega_p^{-1}$. In the rest of the paper, the total fluctuating field energy density is denoted by $\varepsilon = (\delta\mathbf{E}^2 + \delta\mathbf{B}^2)/8\pi$.

3. Results

We first describe the case of $\sigma_r = 6$ (correspondingly $T_{\perp r}/T_{||r} = 4$). Figure 2 displays the linear growth rates from the dispersion solver (using the approximate partial shell of equation (4)). We computed the complex frequency $\omega = \omega_r + i\gamma$ in ψ-k space for the Alfvén-cyclotron (AC) instability (same as in paper 1), but in $k_{||}$-$k_\perp$ space for the ion Bernstein (IB) instability, where ψ is the wave normal angle. The reason for the latter choice is that the complex growth rate pattern is better organized in $k_{||}$-$k_\perp$ space as σ_r approaches zero [cf. *Min and Liu*, 2015b, Figure 7] probably related to the wave-proton resonant condition. In addition, since the IB modes can have multiple dispersion surfaces at different frequencies, we have chosen the maximum growth rate among all dispersion surfaces at given $(k_{||}, k_\perp)$ to produce Figure 2b. The sharp contrast of color intensity between the two panels readily indicates that the growth rates of the AC instability are generally much lower than those of the IB instability. The maximum growth rates of the AC and IB instabilities are, respectively, $\gamma_m^{AC} \approx 0.063\Omega_p$ and $\gamma_m^{IB} \approx 0.143\Omega_p$ (the third harmonic); the locations of the maximum growing modes are marked with the solid dots in the figure.

The PIC simulation results for the case of $\sigma_r = 6$ are shown in Figure 3. Figure 3a displays the time evolution of the simulated field energy density. Also shown in paper 1, the two distinct local maxima are apparent due to the well-separated saturation times of the two instabilities, the first of which corresponds to the IB instability and the second to the AC instability. We label the times at which the two local maxima occur as t^{IB} and t^{AC} and the corresponding total field energy densities as ε^{IB} and ε^{AC}, respectively. For this nominal case, ε^{AC} is slightly larger than ε^{IB}. Figures 3b and 3c display snapshots of the electric (left) and magnetic (right) field power spectra in wave number space at $t = 33\Omega_p^{-1}$ and $150\Omega_p^{-1}$, respectively, which not only verify the linear growth rates shown in Figure 2 but also present two different instabilities contributing to the two local maxima of the field energy density. The snapshots have been taken during the linear growth phases of IB and AC instabilities at times earlier than t^{IB} and t^{AC}, respectively, to demonstrate better agreement of the simulated fluctuations with the linear theory growth rate contours.

We have performed similar linear analyses and PIC simulations for the σ_r values in Table 1. Figure 4 compares (top) the maximum growth rates from linear theory, (middle) the saturation levels of the field energy density from the simulations as a function of σ_r, and (bottom) the saturation levels as a function of the saturation time. Both γ_m^{AC} and γ_m^{IB} are an increasing function of σ_r, which can be understood as follows. As σ_r increases, protons initially uniform in pitch angle space are being concentrated around $v_{||} = 0$ and $v_\perp = v_r$, and therefore, there is more free energy available for both instabilities to grow. Unlike γ_m^{AC} that exhibits a monotonic increase, there exists a plateau in γ_m^{IB} in the range of $6 \le \sigma_r \le 11$.

Note the inequality $\gamma_m^{IB} > \gamma_m^{AC}$ for all σ_r values considered. As shown in paper 1, this relation holds for the anisotropy of the ring protons as large as $T_{\perp r}/T_{||r} = 21.3$ (corresponding to $\sigma_r = 40.6$ in the present study). The saturation levels of the field energy density are also an increasing function of σ_r, but ε^{AC} has steeper slopes for $\sigma_r \gtrsim 2$ while ε^{IB} remains relatively constant. From the figure, the critical anisotropy at which $\varepsilon^{AC} \approx \varepsilon^{IB}$ is $T_{\perp r}/T_{||r} \approx 3$ (or $\sigma_r \approx 4$). Note that one data point of ε^{AC} is missing for $\sigma_r = 0$ because the distribution is fully isotropic and, therefore, stable to the AC instability. In addition, the second peak in the field energy evolution corresponding to AC instability for $\sigma_r = 1$ was just above the background noise level (not shown). Also related

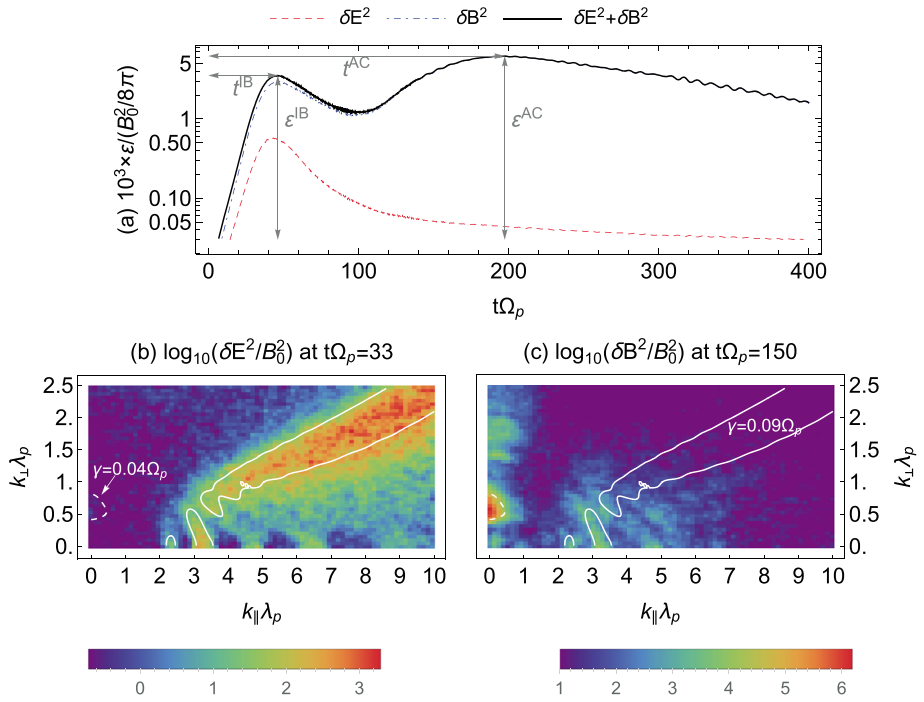

Figure 3. Summary of the PIC simulation results corresponding to the partial shell distribution with $\sigma_r = 6$. (a) Time evolution of the electric (red dashed), magnetic (blue dash-dotted), and total (solid) field energy density normalized to $B_0^2/8\pi$. The first local maximum of the total energy density corresponds to the saturation of the ion Bernstein instability and the second local maximum to the Alfvén-cyclotron instability. (b) Simulated electric field power spectrum at $t = 33\Omega_p^{-1}$ showing the quasi-electrostatic ion Bernstein waves. (c) Simulated magnetic field power spectrum at $t = 150\Omega_p^{-1}$ showing the strongly electromagnetic Alfvén-cyclotron waves. The dashed and solid contours in Figures 3b and 3c delineate the growth rates of $\gamma = 0.04\Omega_p$ and $0.09\Omega_p$ from linear theory, respectively.

to σ_r are t^{AC} and t^{IB} which, as shown in Figure 4 (bottom), appear to be linearly correlated with the logarithms of ε^{AC} and ε^{IB}, respectively (see the linear fits in the figure).

The linear theory results at the maximum growth rates are listed in Table 1. First to note is $\psi_m^{AC} \approx 70°$ at $k_m^{AC}\lambda_p > 1$ for $\sigma_r \lesssim 1$. This oblique AC mode was extensively investigated by *Denton et al.* [1992] using a loss cone proton distribution; they suggested that the oblique AC modes can be an alternative explanation for linearly polarized EMIC waves observed in the inner magnetosphere. The wave normal angle and wave number obtained here are consistent with theirs.

Second, when the partial shell proton distribution is close to an isotropic shell with $\sigma_r < 1.5$, $\psi_m^{IB} \equiv \tan^{-1}(k_{\perp m}^{IB}/k_{||m}^{IB})$ is not exactly, although close to, 90°. This was also shown by *Min and Liu* [2015b] (Figure 7 therein) and can be understood from the results of *Chen* [2015]. In a homogeneous, nondrifting plasma with a uniform background magnetic field $\mathbf{B}_0$ (which has been assumed throughout), if $k_{||} = 0$, the wave-particle interactions are independent of the $v_{||}$ properties of the particle velocity distributions. The effective positive slope of the reduced proton $v_\perp$ distribution determines the growth rate of the perpendicular propagating waves [*Chen*, 2015, equation (6)]. On the other hand, as the wave normal angle ψ decreases from 90°, the waves have a propagation component along $\mathbf{B}_0$ (i.e., $k_{||} \neq 0$) and primarily interact with protons around the cyclotron resonant speeds of $v_{||\mathrm{res}} = (\omega_r - \mu\Omega_p)/k_{||} \sim 0$ [*Chen*, 2015, Figure 3]. So the magnitude of the positive slope of the partial shell around $v_{||} \sim 0$ determines the wave growth rates. Since the effective positive slope of the reduced proton $v_\perp$ distribution is smaller than the local slope around $v_{||} \sim 0$ for a nearly isotropic partial shell distribution, the growth rate of the perpendicularly propagating IB mode is smaller than that of the quasi-perpendicularly propagating mode. However, the situation becomes different for a ring velocity distribution used in paper 1 or for a partial shell distribution with sufficiently large σ_r (e.g., Figure 1c), for which the proton phase space density concentrates around $v_{||} \sim 0$. Then the effective positive slope of the reduced proton $v_\perp$ distribution can become larger than the local slope at $v_{||} \sim 0$.

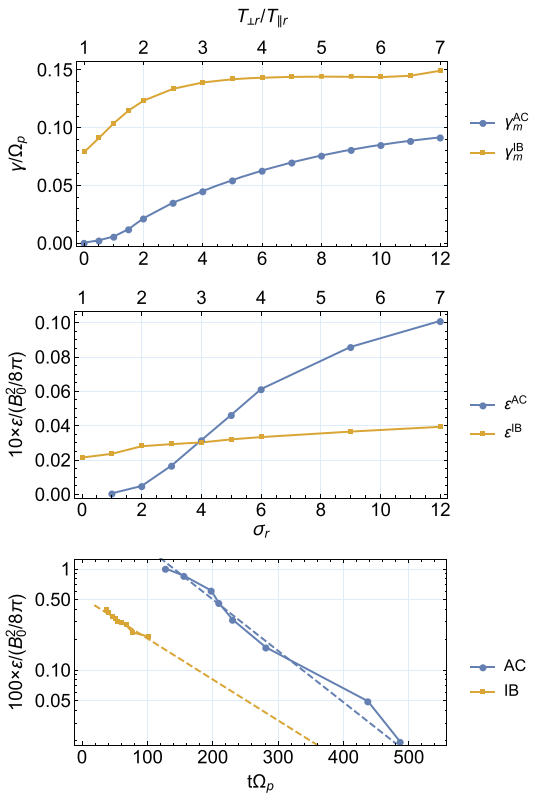

Figure 4. (top) Scalings of the maximum growth rates from linear analyses, (middle) the saturation levels from PIC simulations for the selected σ_r values, and (bottom) relationship between the saturation levels and the saturation times. The blue (orange) curves with solid circles (squares) correspond to the Alfvén-cyclotron (ion Bernstein) instability. The dashed lines in Figure 4 (bottom) are linear fits to the data points for the respective instabilities.

Finally, ψ_m^{IB} approaches 90° for $\sigma_r \gtrsim 1.5$ (the inequality "≤" in the table is because the minimum $k_{||}$ used for root finding in our linear theory analyses was $0.01\lambda_p^{-1}$). At the same time, the growth rate of the IB modes at $\psi \sim 75°$ (the continuous part in Figure 2b) intensifies as the distribution becomes more anisotropic (see supporting information). Consequently, ψ_m^{IB} exhibits the sudden shift to $\sim 75°$ for $\sigma_r \gtrsim 11$, which may explain the plateau of γ_m^{IB} in the range of $6 \lesssim \sigma_r \lesssim 11$ in Figure 4 (top). It is interesting to note that $\psi_m^{IB} \approx 74°$ for proton model 1 in paper 1 (Figure 1 therein), which is effectively equivalent to a partial shell distribution with $\sigma_r \approx 40$ in the present study.

4. Conclusions

Linear dispersion analyses and two-dimensional electromagnetic PIC simulations have been performed to study the linear growth and nonlinear saturation of EMIC and fast magnetosonic waves, which have as their source the Alfvén-cyclotron (AC) and ion Bernstein (IB) instabilities, respectively, driven by a proton partial shell velocity distribution. The scaling of the two instabilities on the temperature anisotropy of the partial shell proton distribution, $T_{\perp r}/T_{||r}$, is examined by varying the anisotropy but with other parameters fixed. For the wide range of anisotropy ($1 \le T_{\perp r}/T_{||r} \le 7$) considered, the maximum growth rate of the IB instability is always larger than that of the AC instability. Yet the latter waves saturate at a larger level as long as $T_{\perp r}/T_{||r} \gtrsim 3$. The reason is that the increase of $T_{\perp r}/T_{||r}$ corresponds to a substantial increase in the free energy available for the AC instability, whereas the increase of the free energy for the IB instability is relatively small (note that the shell speed and the thermal spread of the shell are fixed).

Observations of fast magnetosonic waves are often not accompanied by EMIC waves as discussed in section 1. This suggests that the temperature anisotropy of the proton ring-like distributions associated with the former waves should not be large enough to excite substantial EMIC waves. In the present study, we have varied the effective temperature anisotropy of the partial shell protons but kept the other parameters of the proton ring-like distributions fixed. The results above indicate that if the ring-like proton distributions driving these fast magnetosonic waves have parameters similar to those fixed here, they should be close to isotropic shell distributions with the partial shell proton anisotropy less than 3. This critical temperature anisotropy may vary with the ring speed, the ring thermal speed, and/or the ring density which have been fixed. Further investigation of the dependence on these parameters will be left as a future study.

The fact that a larger linear growth rate does not always correspond to a larger wave saturation amplitude as revealed in the present study serves as a reminder of the limitations of linear theory. One needs to be cautious when comparing linear growth rates with observed wave spectra because they are, although closely related, two different entities. Note that the different saturation levels of the different modes in the simulations discussed are related to their different free energy sources and different amounts of free energy available. They are not caused by the different background noise levels at different frequencies in the simulations. As noted in *Liu et al.* [2011], runs with fewer simulation particles per cell are supposed to have higher noise levels but still yield the same saturation levels for the enhanced waves as long as they saturate well above the noise levels.

Finally, from a general space plasma physics point of view, observations often show that broadband turbulence amplitudes typically decrease as wave frequencies increase and wavelengths decrease, whereas linear dispersion theory predicts that kinetic instability growth rates generally increase with increasing frequencies and decreasing wavelengths [e.g., *Gary*, 1993]. A simple physical picture is that lower frequency waves correspond to greater inertia and therefore have the potential to yield greater fluctuation energy but slower growth rates. In this picture, then, it is not surprising that the Alfvén-cyclotron instability yields larger amplitude fluctuations even though ion Bernstein instabilities may have faster growth rates.

Acknowledgments

Data supporting the figures presented are available upon request from the corresponding author. The work at Auburn University was supported by NASA grant NNX13AD62G and NSF grant 1303623. The research effort of S.P.G. was supported by the NSF-GEM project 1303300, "An Integrated Study of Fast Magnetosonic Waves in the Radiation Belts." Computational resources supporting this work were provided by the NASA High-End Computing (HEC) program through the NASA Advanced Supercomputing (NAS) Division at Ames Research Center. K.M. is grateful to Mark J. Engebretson for discussions, and S.P.G. thanks Lunjin Chen for a very helpful discussion.

References

Allen, R. C., J.-C. Zhang, L. M. Kistler, H. E. Spence, R.-L. Lin, B. Klecker, M. W. Dunlop, M. Andr, and V. K. Jordanova (2015), A statistical study of EMIC waves observed by Cluster: 1. Wave properties, *J. Geophys. Res. Space Physics*, *120*, 5574–5592, doi:10.1002/2015JA021333.

Anderson, B. J., R. E. Erlandson, and L. J. Zanetti (1992), A statistical study of Pc1–2 magnetic pulsations in the equatorial magnetosphere: 1. Equatorial occurrence distributions, *J. Geophys. Res.*, *97*(A3), 3075–3088, doi:10.1029/91JA02706.

Arfken, G. B. (1985), *Mathematical Methods for Physicists*, 3rd ed., Academic Press, Orlando, Fla.

Balikhin, M. A., Y. Y. Shprits, S. N. Walker, L. Chen, N. Cornilleau-Wehrlin, I. Dandouras, O. Santolík, C. Carr, K. H. Yearby, and B. Weiss (2015), Observations of discrete harmonics emerging from equatorial noise, *Nat. Commun.*, *6*, 7703, doi:10.1038/ncomms8703.

Boardsen, S. A., G. B. Hospodarsky, C. A. Kletzing, R. F. Pfaff, W. S. Kurth, J. R. Wygant, and E. A. MacDonald (2014), Van Allen Probe observations of periodic rising frequencies of the fast magnetosonic mode, *Geophys. Res. Lett.*, *41*, 8161–8168, doi:10.1002/2014GL062020.

Bortnik, J., and R. M. Thorne (2010), Transit time scattering of energetic electrons due to equatorially confined magnetosonic waves, *J. Geophys. Res.*, *115*, A07213, doi:10.1029/2010JA015283.

Chen, L. (2015), Wave normal angle and frequency characteristics of magnetosonic wave linear instability, *Geophys. Res. Lett.*, *42*(12), 4709–4715, doi:10.1002/2015GL064237.

Chen, L., R. M. Thorne, V. K. Jordanova, C.-P. Wang, M. Gkioulidou, L. Lyons, and R. B. Horne (2010a), Global simulation of EMIC wave excitation during the 21 April 2001 storm from coupled RCM-RAM-HOTRAY modeling, *J. Geophys. Res.*, *115*, A07209, doi:10.1029/2009JA015075.

Chen, L., R. M. Thorne, V. K. Jordanova, and R. B. Horne (2010b), Global simulation of magnetosonic wave instability in the storm time magnetosphere, *J. Geophys. Res.*, *115*, A11222, doi:10.1029/2010JA015707.

Chen, L., A. Maldonado, J. Bortnik, R. M. Thorne, J. Li, L. Dai, and X. Zhan (2015), Nonlinear bounce resonances between magnetosonic waves and equatorially mirroring electrons, *J. Geophys. Res. Space Physics*, *120*, 6514–6527, doi:10.1002/2015JA021174.

Clausen, L. B. N., J. B. H. Baker, J. M. Ruohoniemi, and H. J. Singer (2011), EMIC waves observed at geosynchronous orbit during solar minimum: Statistics and excitation, *J. Geophys. Res.*, *116*, A10205, doi:10.1029/2011JA016823.

Cornwall, J. M. (1965), Cyclotron instabilities and electromagnetic emission in the ultra low frequency and very low frequency ranges, *J. Geophys. Res.*, *70*(1), 61–69, doi:10.1029/JZ070i001p00061.

Denton, R., M. Hudson, and I. Roth (1992), Loss-cone-driven ion cyclotron waves in the magnetosphere, *J. Geophys. Res.*, *97*(A8), 12,093–12,103, doi:10.1029/92JA00954.

Denton, R. E., M. J. Engebretson, A. Keiling, A. P. Walsh, S. P. Gary, P. M. E. Décréau, C. A. Cattell, and H. Rème (2010), Multiple harmonic ULF waves in the plasma sheet boundary layer: Instability analysis, *J. Geophys. Res.*, *115*, A12224, doi:10.1029/2010JA015928.

Fraser, B. J., and T. S. Nguyen (2001), Is the plasmapause a preferred source region of electromagnetic ion cyclotron waves in the magnetosphere?, *J. Atmos. Sol. Terr. Phys.*, *63*(11), 1225–1247, doi:10.1016/S1364-6826(00)00225-X.

Fraser, B. J., R. S. Grew, S. K. Morley, J. C. Green, H. J. Singer, T. M. Loto'aniu, and M. F. Thomsen (2010), Storm time observations of electromagnetic ion cyclotron waves at geosynchronous orbit: GOES results, *J. Geophys. Res.*, *115*, A05208, doi:10.1029/2009JA014516.

Gary, S. P. (1993), *Theory of Space Plasma Microinstabilities*, Cambridge Univ. Press, New York.

Gary, S. P., K. Liu, D. Winske, and R. E. Denton (2010), Ion Bernstein instability in the terrestrial magnetosphere: Linear dispersion theory, *J. Geophys. Res.*, *115*, A12209, doi:10.1029/2010JA015965.

Gary, S. P., K. Liu, and D. Winske (2011), Bernstein instability driven by suprathermal protons in the ring current, *J. Geophys. Res.*, *116*, A08215, doi:10.1029/2011JA016543.

Gary, S. P., K. Liu, and L. Chen (2012), Alfvén-cyclotron instability with singly ionized helium: Linear theory, *J. Geophys. Res.*, *117*(A8), A08201, doi:10.1029/2012JA017740.

Halford, A. J., B. J. Fraser, and S. K. Morley (2010), EMIC wave activity during geomagnetic storm and nonstorm periods: CRRES results, *J. Geophys. Res.*, *115*, A12248, doi:10.1029/2010JA015716.

Horne, R. B., G. V. Wheeler, and H. S. C. K. Alleyne (2000), Proton and electron heating by radially propagating fast magnetosonic waves, *J. Geophys. Res.*, *105*(A12), 27,597–27,610, doi:10.1029/2000JA000018.

Horne, R. B., R. M. Thorne, S. A. Glauert, N. P. Meredith, D. Pokhotelov, and O. Santolík (2007), Electron acceleration in the Van Allen radiation belts by fast magnetosonic waves, *Geophys. Res. Lett.*, *34*, 17107, doi:10.1029/2007GL030267.

Hrbáčková, Z., O. Santolík, F. Němec, E. Macúšová, and N. Cornilleau-Wehrlin (2015), Systematic analysis of occurrence of equatorial noise emissions using 10 years of data from the Cluster mission, *J. Geophys. Res. Space Physics*, *120*, 1007–1021, doi:10.1002/2014JA020268.

Kennel, C. F., and H. E. Petschek (1966), Limit on stably trapped particle fluxes, *J. Geophys. Res.*, *71*(1), 1–28, doi:10.1029/JZ071i001p00001.

Liu, K., S. P. Gary, and D. Winske (2011), Excitation of magnetosonic waves in the terrestrial magnetosphere: Particle-in-cell simulations, *J. Geophys. Res.*, *116*, A07212, doi:10.1029/2010JA016372.

Ma, Q., W. Li, R. M. Thorne, and V. Angelopoulos (2013), Global distribution of equatorial magnetosonic waves observed by THEMIS, *Geophys. Res. Lett.*, *40*, 1895–1901, doi:10.1002/grl.50434.

Mauk, B. H., N. J. Fox, S. G. Kanekal, R. L. Kessel, D. G. Sibeck, and A. Ukhorskiy (2013), Science objectives and rationale for the Radiation Belt Storm Probes mission, *Space Sci. Rev.*, *179*, 3–27, doi:10.1007/s11214-012-9908-y.

McClements, K. G., R. O. Dendy, and C. N. Lashmore-Davies (1994), A model for the generation of obliquely propagating ULF waves near the magnetic equator, *J. Geophys. Res.*, *99*(A12), 23,685–23,693, doi:10.1029/94JA01979.

Meredith, N. P., R. B. Horne, and R. R. Anderson (2008), Survey of magnetosonic waves and proton ring distributions in the Earth's inner magnetosphere, *J. Geophys. Res.*, *113*, A06213, doi:10.1029/2007JA012975.

Min, K., and K. Liu (2015a), Regime transition of ion Bernstein instability driven by ion shell velocity distributions, *J. Geophys. Res. Space Physics*, *120*, 8448–8454, doi:10.1002/2015JA021514.

Min, K., and K. Liu (2015b), Fast magnetosonic waves driven by shell velocity distributions, *J. Geophys. Res. Space Physics*, *120*, 2739–2753, doi:10.1002/2015JA021041.

Min, K., and K. Liu (2016), Proton velocity ring-driven instabilities in the inner magnetosphere: Linear theory and particle-in-cell simulations, *J. Geophys. Res. Space Physics*, *121*, 475–491, doi:10.1002/2015JA022042.

Min, K., J. Lee, K. Keika, and W. Li (2012), Global distribution of EMIC waves derived from THEMIS observations, *J. Geophys. Res.*, *117*, A05219, doi:10.1029/2012JA017515.

Němec, F., O. Santolík, K. Gereová, and E. Macúšová (2005), Initial results of a survey of equatorial noise emissions observed by the Cluster spacecraft, *Planet. Space Sci.*, *53*(1–3), 291–298.

Němec, F., O. Santolík, K. Gereová, E. Macúšová, and H. Laakso (2006), Equatorial noise: Statistical study of its localization and the derived number density, *Adv. Space Res.*, *37*(3), 610–616.

Němec, F., O. Santolík, J. S. Pickett, Z. Hrbáčková, and N. CornilleauWehrlin (2013), Azimuthal directions of equatorial noise propagation determined using 10 years of data from the Cluster spacecraft, *J. Geophys. Res. Space Physics*, *118*, 7160–7169, doi:10.1002/2013JA019373.

Perraut, S., A. Roux, P. Robert, R. Gendrin, J.-A. Sauvaud, J.-M. Bosqued, G. Kremser, and A. Korth (1982), A systematic study of ULF waves above f_{H+} from GEOS 1 and 2 measurements and their relationships with proton ring distributions, *J. Geophys. Res.*, *87*(A8), 6219–6236, doi:10.1029/JA087iA08p06219.

Posch, J. L., M. J. Engebretson, C. N. Olson, S. A. Thaller, A. W. Breneman, J. R. Wygant, S. A. Boardsen, C. A. Kletzing, C. W. Smith, and G. D. Reeves (2015), Low-harmonic magnetosonic waves observed by the Van Allen Probes, *J. Geophys. Res. Space Physics*, *120*, 6230–6257, doi:10.1002/2015JA021179.

Rodger, C. J., A. T. Hendry, M. A. Clilverd, C. A. Kletzing, J. B. Brundell, and G. D. Reeves (2015), High-resolution in-situ observations of electron precipitation-causing EMIC waves, *Geophys. Res. Lett.*, *4*, 9633–9641, doi:10.1002/2015GL066581.

Saikin, A. A., J.-C. Zhang, R. C. Allen, C. W. Smith, L. M. Kistler, H. E. Spence, R. B. Torbert, C. A. Kletzing, and V. K. Jordanova (2015), The occurrence and wave properties of H^+-, He^+-, and O^+-band EMIC waves observed by the Van Allen Probes, *J. Geophys. Res. Space Physics*, *120*, 7477–7492, doi:10.1002/2015JA021358.

Santolík, O., F. Němec, K. Gereová, E. Macúšová, Y. de Conchy, and N. Cornilleau-Wehrlin (2004), Systematic analysis of equatorial noise below the lower hybrid frequency, *Ann. Geophys.*, *22*(7), 2587–2595, doi:10.5194/angeo-22-2587-2004.

Thorne, R. M. (2010), Radiation belt dynamics: The importance of wave-particle interactions, *Geophys. Res. Lett.*, *37*, L22107, doi:10.1029/2010GL044990.

Usanova, M. E., I. R. Mann, J. Bortnik, L. Shao, and V. Angelopoulos (2012), THEMIS observations of electromagnetic ion cyclotron wave occurrence: Dependence on AE, SYMH, and solar wind dynamic pressure, *J. Geophys. Res.*, *117*, A10218, doi:10.1029/2012JA018049.

Xiao, F., Q. Zhou, Y. He, C. Yang, S. Liu, D. N. Baker, H. E. Spence, G. D. Reeves, H. O. Funsten, and J. B. Blake (2015), Penetration of magnetosonic waves into the plasmasphere observed by the Van Allen Probes, *Geophys. Res. Lett.*, *42*, 7287–7294, doi:10.1002/2015GL065745.

Zhou, Q., et al. (2014), Excitation of nightside magnetosonic waves observed by Van Allen Probes, *J. Geophys. Res. Space Physics*, *119*, 9125–9133, doi:10.1002/2014JA020481.